crystals

MDPI

Article

Further Insights into the Crystal Engineering of High Explosives of 1:2 Salts of the s-Tetrazine Receptor-Picrate Anion Series

Matteo Savastano [1,*], María Dolores López de la Torre [2], Marco Pagliai [3], Giovanna Poggi [3,4], Francesca Ridi [3,4], Carla Bazzicalupi [3,*], Manuel Melguizo [2,*] and Antonio Bianchi [3,*]

[1] Department for the Promotion of Human Science and Quality of Life, University San Raffaele Roma, Via di Val Cannuta 247, 00166 Rome, Italy
[2] Department of Inorganic and Organic Chemistry, University of Jaén, 23071 Jaén, Spain
[3] Department of Chemistry "Ugo Schiff", University of Florence, Via della Lastruccia 3, 50019 Sesto Fiorentino, Italy
[4] CSGI, University of Florence, Via della Lastruccia 3, 50019 Sesto Fiorentino, Italy
* Correspondence: matteo.savastano@uniroma5.it (M.S.); carla.bazzicalupi@unifi.it (C.B.); mmelgui@ujaen.es (M.M.); antonio.bianchi@unifi.it (A.B.)

Abstract

Both s-tetrazine and picric acid are widely known compounds in the realm of high-energy materials. We had previously taken an interest—mostly supramolecular, i.e., directed at the elucidation of lone pair–π interactions—in the crystal packing of phases containing s-tetrazine-based cations and picrate anions. Herein we report two novel compounds of this family: $H_2L4(picr)_2$ and $(H_2L5)_2(picr)_4$; the former is a polymorph of a previously reported compound of a homologous host series (3,6-bis(4-morpholinobutyl)-1,2,4,5-tetrazine), the latter a salt of the commercially available 3,6-di(pyridin-4-yl)-1,2,4,5-tetrazine. The new phases were investigated via XRD: main interactions, crystal packing, and potential slip planes are discussed. Thermal analysis (DSC/TGA) was conducted for L5 and $(H_2L5)_2(picr)_4$. Enthalpies of formation (thermochemical cycles/DFT) and in silico explosion parameters (EXPLO5) are reported for all compounds. Overall, the data herein reported improve the understanding of the correlation among supramolecular/packing details and the resulting explosive properties.

Keywords: s-tetrazine; picrate; explosives; crystal engineering; supramolecular interactions; thermochemistry; lone pair–π interactions; anion–π interactions; π–hole interactions

Academic Editor: Thomas M. Klapötke

Received: 15 December 2025
Revised: 2 January 2026
Accepted: 4 January 2026
Published: 12 January 2026

1. Introduction

In recent years, the s-tetrazine core has garnered significant attention for a wide variety of applications. Some of them, perhaps the first recognized, stem from the fact that it is aflat H,C,N aromatic with a high N/C ratio; this makes it eligible for use in pyrotechnic, explosive and even designed high-energy materials [1–3]. In the realm of synthetic chemistry, it is nowadays recognized as an attractive 2,3 diazadiene [4] as well as a useful moiety in biorthogonal derivatives [5,6]. The s-tetrazine moiety is increasingly used in redox-based devices [7–11] and redox-driven applications [12,13] due to its π*-centered LUMO and its generally redox-reversible behavior. Finally, as we plentily demonstrated, due to its positive Q_{zz} ring quadrupolar moment and the strong anion–π interactions it can generate, the s-tetrazine ring can be effectively exploited in the design of receptors for anions [14,15].

We have previously explored in depth the possibilities in the anion coordination realm, showing the invariable formation of strong and centered anion–π interactions (with inorganic anions) [14–19], strong and centered π–π stacking with electron rich aromatics (e.g., benzen-, mono-, and di-carboxylates) [20] or, if no better nucleophilic site is available on the guest, centered lone pair–π interactions (e.g., in the packing modes of s-tetrazine based ligands themselves) [14,21].

The above studies were conducted for a series of s-tetrazine-based receptors (L1–L4, Scheme 1) that we devised. These are decorated with morpholinic pendants, acting both as protonable sites able to ensure the ligands' water solubility and as additional binding sites for the anions via salt-bridging. The variable arm length was used to forcibly tune (up or down) the possible cooperativity between salt-bridges and aromatic (anion–π, π–π, lone pair–π) interactions, leading to a deep understanding of the fine balance of supramolecular forces in solution and in the solid state.

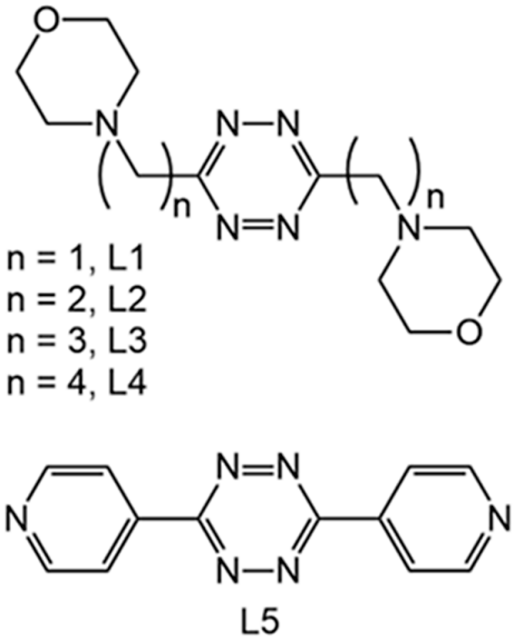

Scheme 1. The s-tetrazine based receptors discussed in this study. L1: 3,6-bis(morpholinomethyl)-1,2,4,5-tetrazine; L2: 3,6-bis(2-morpholinoethyl)-1,2,4,5-tetrazine; L3: 3,6-bis(3-morpholinopropyl)-1,2,4,5-tetrazine; L4: 3,6-bis(4-morpholinobutyl)-1,2,4,5-tetrazine; L5: 3,6-di(pyridin-4-yl)-1,2,4,5-tetrazine.

In an effort of showing full control over the interactions that the s-tetrazine ring will engage into in crystalline phases, we demonstrated how it is indeed possible to choose a substrate which is (i) an anion, (ii) an aromatic molecule, and (iii) a species possessing lone pair-bearing atoms and still have its complexes with the s-tetrazine ligands preferring and displaying lone pair–π interactions over anion–π or π–π ones [21].

While this behavior is in principle surprising (in general terms the other interactions are stronger than lone pair–π ones), as we demonstrated, it can be achieved by a conscious choice of the stereoelectronic features of the guest molecule; in our sample case, the picrate anion. The picrate anion interacts with diprotonated L1–L4 ligands always displaying lone pair–π interactions. This happens because of the high propensity of its phenolate-type anionic site to form salt-bridges with the morpholinium sites, rather than anion–π interactions. Likewise, the very electron deficient nature of the π-system of picrate discourages π–π contacts with the likewise electropositive s-tetrazine ring. As a matter of fact, with this choice of substrate, the displayed interactions could be steered away from

anion–π and π–π interactions towards the less stabilizing in the general case, lone pair–π interactions [21].

Of course, selection of picrate anion and its pairing with s-tetrazine ligands, both kinds of derivatives being commonly used in the field of high-energy materials, triggered a more in-depth study of the thermogravimetric and explosive properties of the resulting crystalline phases. Interestingly, the DSC/TGA/DTG determined kinetic parameters for thermal (explosive) decomposition (both preexponential factor and activation energy, and thus the whole rate constant k) were found to be a linear function of picrate–picrate contacts in the crystals [21].

This is a conceptually interesting finding, which, however, cannot be hastily extended, as this was proven valid only for a series of crystals containing the same main interactions, moreover, with a homologous series of receptors. Still, as commented, it offers a unique perspective on the crystal engineering of high energy materials.

In this study, we intended to address a simple s-tetrazine commercial derivative, L5 (Scheme 1). This features an extended aromatic framework and a N/C ratio equal to that of L2 (the second-highest in the previously investigated series), and its completely flat nature is also in line with the standard design principles of high explosives (i.e., aimed at having "easy" slip planes, less prone to molecular frictions capable to initiate an involuntary explosive discharge of the energy stored in the material) [22–26].

As the study proceeded, it happened that we also isolated a different picrate salt of diprotonated L4, a different polymorph. In principle, polymorphism is a sensible possibility, especially for the more conformationally flexible (longer alkyl chains) L4 receptor, and due to the deliberate "balance of supramolecular forces" design we used to promote the prevalence of weak lone pair–π interaction in the system. Still, as we will reason, the new crystalline phase opens up to a few interesting considerations as it is the only known crystal structure of these ligands (after a total of ≈ 30 different CSD depositions) where only one face of the s-tetrazine moiety is engaged in the interaction with the substrate.

2. Materials and Methods

All reagents were high purity compounds and were purchased from Sigma-Aldrich, except for L5, whose supplier was TCI.

L4 was obtained as previously described [16].

H_2L4(picr)$_2$ crystals were obtained as previously described, both by evaporation and diffusion methods [21].

After the initial discharge and crystallization of the H_2L4(picr)$_2$ main compound, upon evaporation, the saturated solution of L4 and picric acid kept affording some crystals.

Upon optical inspection, among the familiar prismatic ones of the known compound, a few isometric crystals were found. These were hand-picked, mounted, and subjected to XRD studies.

(H_2L5)$_2$(picr)$_4$ crystals are very poorly soluble, causing a hasty and disorganized precipitation of microcrystalline product in direct mixing experiments. Therefore, crystals were patiently grown with the described diffusion technique employed to obtain high quality crystals of L1–L4 [21].

2.1. X-Ray Structure Analyses

Dark orange crystals of H_2L4(picr)$_2$ and (H_2L5)$_2$(picr)$_4$ were analyzed. The quality of both samples was limited, but sufficient for X-ray diffraction analyses. A summary of the crystallographic data is reported in Table S1. The integrated intensities were corrected for Lorentz and polarization effects, and an empirical absorption correction was applied [27]. The structures were solved by direct methods (SHELXS-97) [28]. Refinements were per-

formed by means of full-matrix least-squares using SHELXL Version 2014/7 [29]. All of the non-hydrogen atoms were anisotropically refined. Hydrogen atoms were introduced in calculated positions and their coordinates were refined according to the linked atoms.

CCDC 2515280 ($H_2L4(picr)_2$) and 2515281 ($(H_2L5)_2(picr)_4$) contain the supplementary crystallographic data for this study.

2.2. Thermal Analysis

The analysis was conducted with a TA Instruments SDT Q650 (TA Instruments, New Castle, DE, USA), which allows for the simultaneous monitoring of the weight loss signal (TGA curve and its derivative, i.e., DTG curve) and the heat flow profile (DSC curve). Samples were placed in an alumina pan and measured in N_2 atmosphere (flow rate 100 mL/min) from room temperature to 600 °C. Thermal profiles of ligands (L1–L5) and picric acid (PA) were acquired at 10 °C/min, while those of their picrate complexes were recorded at different scan rates (5, 10, 20, 50 °C/min).

2.3. Calculated Heats of Formation

Heat of formation is among the key parameters for high-energy materials. Heats of formation for the studied picrate complexes were obtained using the general procedure described in detail in a previous work [21].

The method uses a mixture of thermodynamic (Born–Haber) cycles, isodesmic reactions, incremental methods (to account for the increasing number of -CH_2- groups in the side chains), DFT calculations, and experimental (crystallographic) data such as stoichiometries, molecular weights, and crystal density [30].

In the case of the new L4 complex only crystallographic data were changed, while the rest of the parameters remained as in ref. [21].

In the case of the picrate complex of L5, the Born–Haber cycle is as follows (Scheme 2):

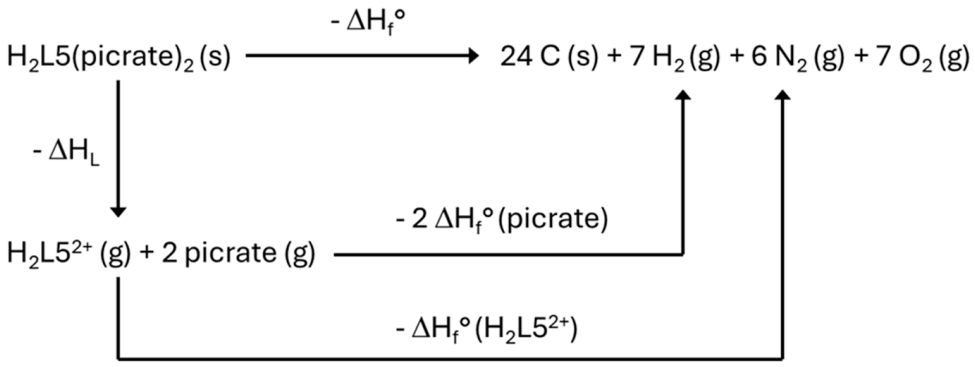

Scheme 2. Employed Born–Haber cycle for the evaluation of the enthalpy of formation of the L5 picrate complex.

The employed isodesmic reaction is as shown in Equation (1):

$$H_2L5^{2+} + 2\,CH_4 \longrightarrow \text{s-tetrazine} + 2\ \text{4-methylpyridinium} \quad (1)$$

Equation (1) was used to calculate the ΔH_f^0 for the H_2L5^{2+} cation as the difference between the calculated reaction ΔH_{reaz} (298 K) (see Section 2.4 for details) and the ΔH_f^0 values of CH_4 [31] and s-tetrazine [32]. The ΔH_f^0 of 4-methylpyridinium was worked out using a thermodynamic cycle from NIST [33] data. In more detail, employed data were ΔH_f^0 of 4-methylpyridine in the gas phase [34], ΔH_f^0 of H^+ in the gas phase [35], and proton affinity of 4-methylpyridine in the gas phase [36].

Concerning the ΔH_L value, this was calculated using Equation (2) [30]:

$$\Delta H_L = U_{pot} + \left[p\left(\frac{n_{cat}}{2} - 2\right) + q\left(\frac{n_{an}}{2} - 2\right)\right]RT \quad (2)$$

as the sum of U_{pot} (lattice energy) and the PΔV term.

The latter is calculated as per Equation (2), taking into account the "shape" (monoatomic, linear polyatomic, non-linear polyatomic) of the cations and anions (n_{cat} and n_{an} coefficients), and their charges (p and q) [30].

The U_{pot} main term is calculated from Equation (3) [30]:

$$U_{pot} = \gamma\left(\frac{\rho}{M_w}\right)^{1/3} + \delta \quad (3)$$

where ρ is the density of the material (g/cm^3), M_w is the compound molecular weight (g/mol) and γ and δ (kJ) are tabulated, salt-stoichiometry dependent, coefficients [30].

2.4. Density Functional Theory Calculations

Density functional theory (DFT) calculations were carried out with the Gaussian 09 suite of programs [37]. Gas phase energy values at 0 K (M062X/cc-pVTZ basis set [38,39]), were added of the zero-point energy and thermal factors up to 298 K. All reactants and products were optimized and characterized as true local minima on the potential-energy surface by frequence analysis. Input coordinates for H_2L5^{2+} were taken from the $H_2L5(picrate)_2$ crystal structure.

2.5. Structure Analysis

Displayed Hirshfeld surfaces were calculated with CrystalExplorer21 [40].

CCDC Mercury was used for displaying purposes and investigation of the features of candidate slip planes [41].

3. Results and Discussion

3.1. Crystal Structure of $(H_2L5)_2(Picr)_4$

The crystal structure of the picrate salt of the diprotonated H_2L5^{2+} ligand is the most complex obtained so far in the series.

We commented previously for the picrate complexes of the homologous ligands L1–L4 an odd–even behavior, where ligands with an odd number of C atoms in the bridge (H_2L1^{2+} and H_2L3^{2+}) give centrosymmetric structures containing only half ligand and 1 anion in the asymmetric unit, while their even counterparts (H_2L2^{2+} and H_2L4^{2+}) present a full ligand and its 2 counteranions [21].

In the case of L5, we instead observed the presence of 2 non-symmetry related H_2L5^{2+} ligands and 4 non-symmetry related picrate anions. An overview of the asymmetric unit is provided in Figure 1.

Given the supramolecular and energy material focus, both the molecular interactions details and overall packing features are worthy of discussion.

Although slightly different, the environments of the two non-symmetry related ligands appear very similar.

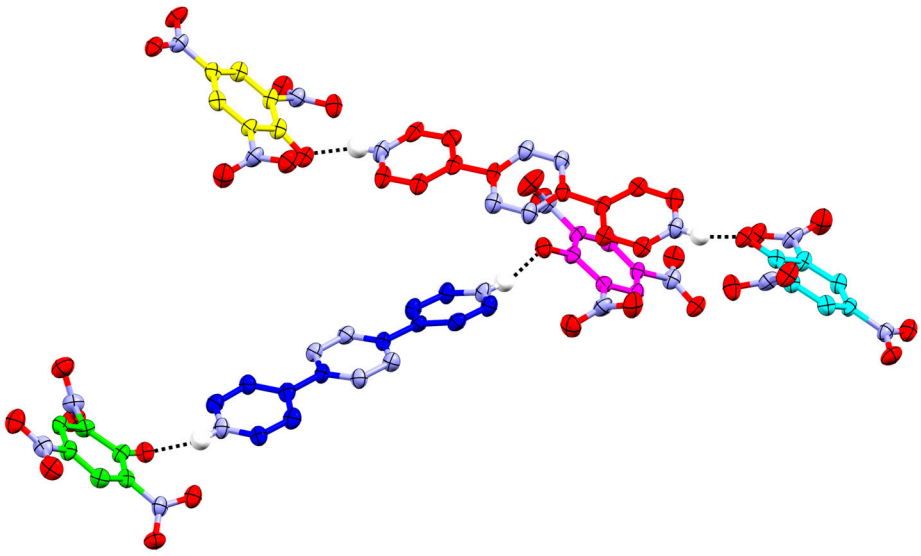

Figure 1. View of the asymmetric unit of $(H_2L5)_2(picr)_4$ crystals. The non-symmetry related red/blue deprotonated ligands are interact via linear salt-bridges with pairs of picrate anions (red ligand, yellow and cyan anions; blue ligand, green and magenta anions), mostly via the phenolate anionic site. Only H atoms involved in salt-bridges are explicitly shown.

The red ligand is surrounded by all the four non-symmetry related anions, interacting either via salt-bridges or anion–π/lone pair–π contacts, as evidenced by its Hirshfeld surface (Figure 2).

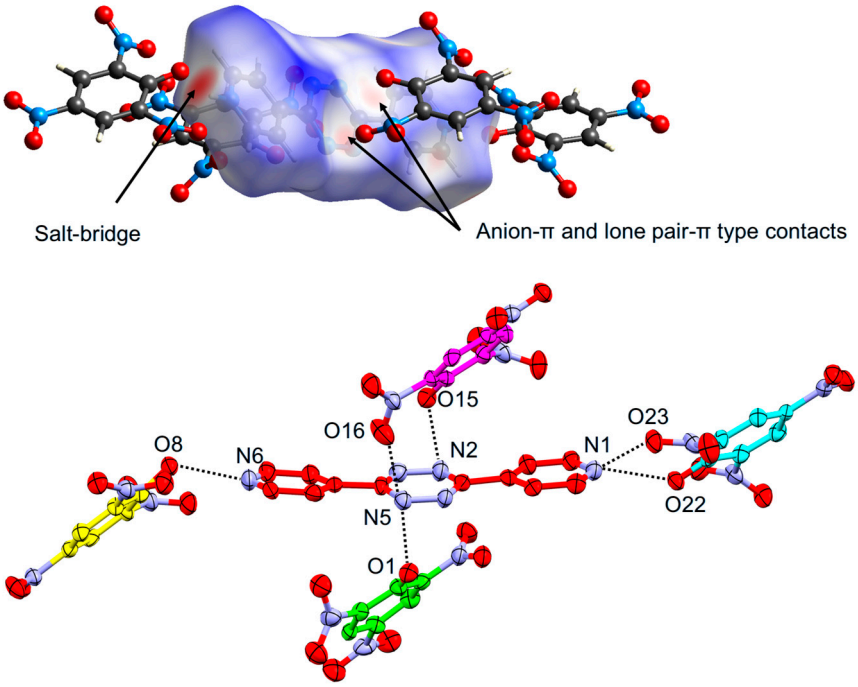

Figure 2. Top: Hirshfeld surface of the red ligand in the $(H_2L5)_2(picr)_4$ crystals, showing pyridinium-phenolate salt-bridges, anion–π and lone pair–π interactions as the most noticeable forces governing the crystal packing. Bottom: Details of short intramolecular contacts and labels of the interacting atoms. Hydrogen atoms omitted for clarity.

The yellow (N6···O8 2.608(6) Å) and cyan (N1···O22 2.622(7) Å) picrate anions form strong and linear pyridinium-phenolate salt-bridges, with some further participation of a nitro group oxygen atom in the case of the cyan anion (N1···O23 2.996(9) Å).

The green and magenta picrate anions, which are both engaged in pyridinium-phenolate salt-bridges with the blue ligand, interact with the red ligand via anion–π (green, O1···N5 2.957(9) Å, magenta, O15···N2 3.01(1) Å) and lone pair–π interactions (magenta, O16···N5 2.81(1) Å). As for the fact that the lone pair–π contact is found to be shorter than the anion–π ones, we remind how the phenolate sites are engaged in salt-bridging with the blue ligand. The above details can be appreciated in Figure 2.

The same considerations are valid for the closely related environment for the blue ligand.

In this case, the "pairs" of anions surrounding it appear just swapped, with the green and magenta ones involved into pyridinium-phenolate salt-bridges (green, N12···O1 2.621(8) Å, magenta, N7···O15 2.65(1) Å) and the cyan and yellow in anion–π type interactions with one or the other face of the s-tetrazine ring (yellow, O8. . .N10 2.819(8) Å, cyan, O22···N9 3.017(8) Å, O22···N113.051(8) Å). The close similarity of the red and blue ligand environments can be appreciated by comparing Figure S1 and Figure 2.

As for global packing, the crystals can be qualitatively described as π-stacks of picrate anions (head to tail, face to face π–π stacking) paneled by the cationic ligands. This is particularly manifest in the view along the b direction, as presented in Figure 3a. The mutual disposition of ligands is better clarified in Figure 3b (viewed along the c axis), where a herringbone motif, in which the red and blue ligands give rise to a certain zigzag motive due to pyridine–pyridine contacts, can be appreciated.

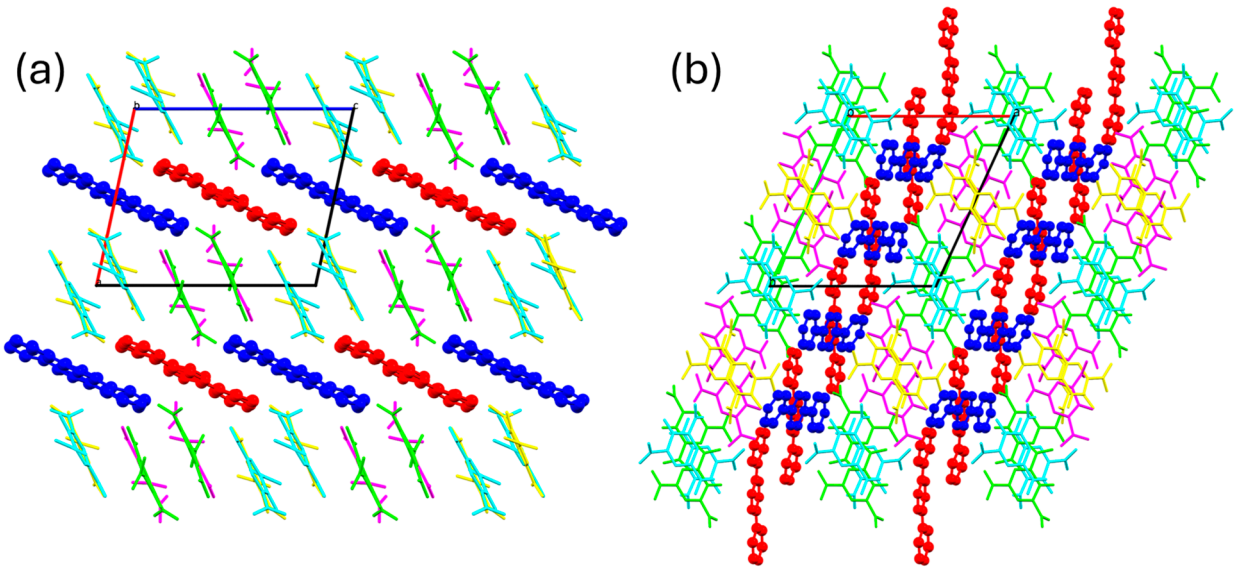

Figure 3. Views of the packing of the $(H_2L5)_2(Picr)_4$ crystals. (**a**) View along the *b*-axis, highlighting picrate–picrate molecular stacks. (**b**) View along the *c*-axis highlighting the herringbone disposition of the ligands. Color code is retained from the above discussion, stick representation is used for anions and a ball and stick one for ligands.

Importance of slip-planes, and especially of the lack of high interpenetration among slabs and/or the necessity of breaking strong directional interactions in the slipping process, are acknowledged for high-energy materials [22,24–26]. In general, materials capable of dissipating physical shocks without generating significant friction and temperature hotspots are safer, i.e., less prone to unintended self-initiation. Nature of the subtending inter-slab forces appears to play a key role [42–44].

In the case of the present crystal structure, the less interpenetrating slip plane belongs to the (100) family. However, this plane displays a honeycomb-like topological structure (in

terms of relative depths and bulges), and slipping would imply rupture of the salt-bridges (strongest interactions) (Figure 4).

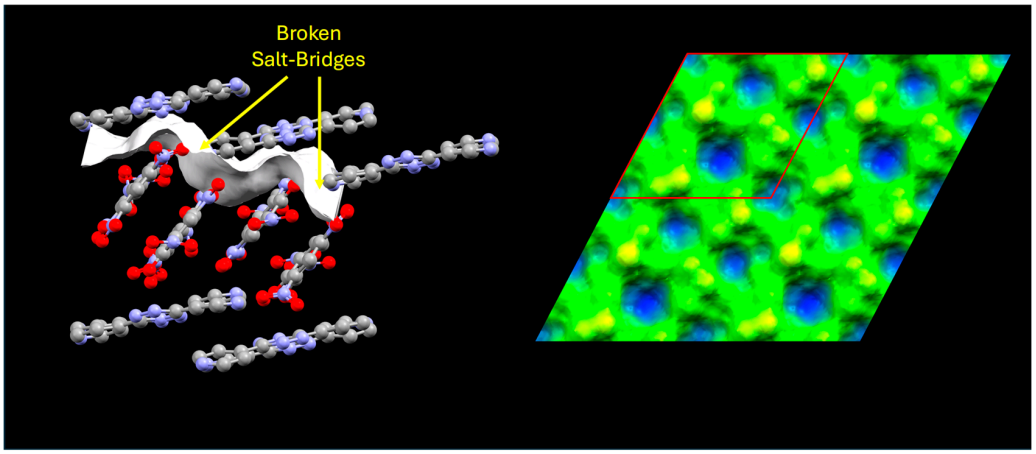

Figure 4. The slip plane of the (100) family in the $(H_2L5)_2(Picr)_4$ crystals, showing the lowest interpenetration. Topology of the surface reveals that salt-bridges need to be broken upon slipping as they correspond to the blue depth maxima (left). A more enlarged view of the topology of the plane (right) (4 × 4, red contour represents the portion showed on the left) showcases a honeycomb-type network where some molecular crashes and the possibility of breaking and reforming of salt-bridges are envisaged during the sliding process. These phenomena are generally understood to cause significant friction at the molecular level.

A far better option appears to be the slip plane of the family (30–2). This has a higher-yet-reasonable slab interpenetration (the second lowest in the crystal), but slipping requires only the sliding of aromatic surfaces onto one another, with no cleavage of the salt-bridges required (Figure 5). Beyond some terracing, the relative bulges and depths onto this plane are due to lone pair–π type contacts only, which admittedly have a lessened energy content with respect to salt-bridges. Therefore, the rugosity of this plane is comparatively lower. Also, the repeat frequency (in terms of spatial separation of the planes) of this latter slip plane is more than 3 times higher with respect to the former one, perhaps better allowing from a bulk shear mode dissipation of mechanical stress (i.e., a deck of cards-like response to mechanical stress). A comparison of the features of both considered slip planes is offered in Table 1.

Table 1. Comparative features of the more relevant slip-plane candidates in the $(H_2L5)_2(Picr)_4$ crystals.

Slip Plane	Less Interpenetrated	Proposed Best Candidate
Orientation	(100)	(30–2)
Offset (Å) [a]	+3.617	0.000
Slab Separation (Å) [b]	−0.644	−1.143
Repeat Distance (Å)	11.681	3.762
Salt-Bridges	Yes	No
Rugosity [c]	1.412	1.192

[a] Offset in the normal direction with respect to the plane family specified as "Orientation". [b] Distance of adjacent slabs through the slip planes (negative values indicate layer interpenetration). [c] Ratio of "real" (1.2 Å probe, 0.3 Å grid spacing) surface area to projected "geometrical" area.

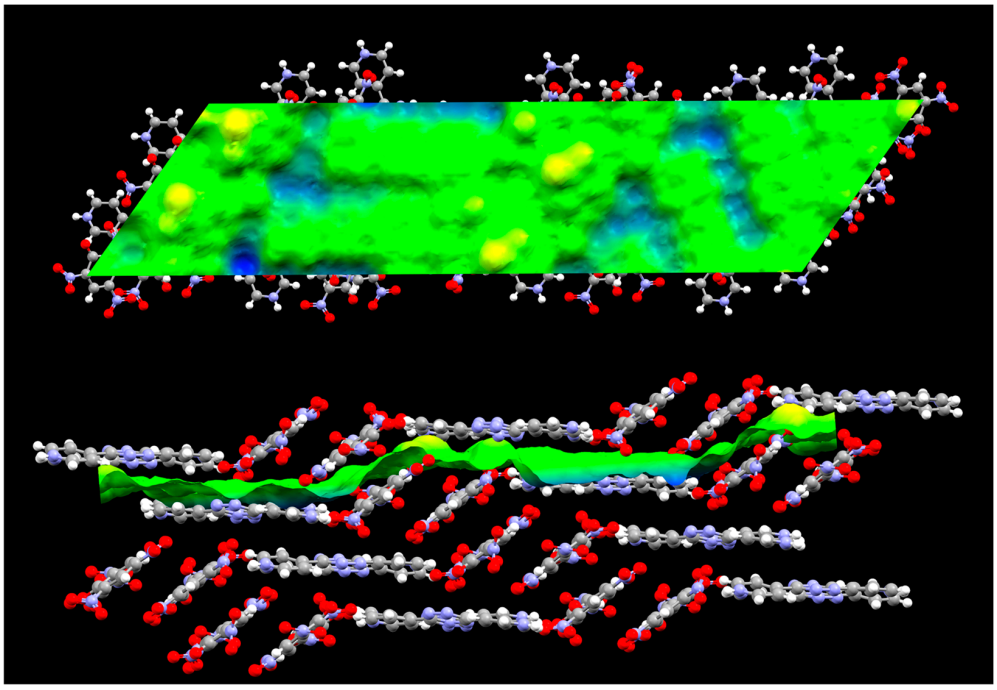

Figure 5. The best candidate slip plane in $(H_2L5)_2(Picr)_4$ crystals, belonging to the (30–2) family. Sliding on this plane does not require breaking of any salt-bridge (top) and can be mostly viewed as two π-surfaces sliding on top of one another. While there is some rugosity, this is mostly due to the terracing nature of the plane rather than to the actual blue depths, which are associated with lone pair–π type contacts.

No logical slip planes with superior features could be reliably detected for this crystal structure.

A comparative summary of the mentioned slip planes can be found in Table 1.

3.2. Crystal Structure of a New Polymorph of $H_2L4(Picr)_2$

A crystal structure of the $H_2L4(Picr)_2$ complex was previously reported [21].

Upon evaporation over time, as can be expected, the mother solution from which the crystals were obtained continued to afford a few crystals. Interestingly, a small minority of these later obtained crystals have a different habitus. For this reason, they were manually picked and further investigated via XRD. This confirmed the formation of a new polymorph of the reported compound.

The different spatial arrangements of ligand and anions in the asymmetric units of the two polymorphs can be comparatively appreciated from Figure 6. The main interactions remain of the same kind: 2 strong salt-bridges per ligand molecule (N6···O10 and N1···O3, 2.686(8) and 2.73(1) Å, respectively), and, regarding the s-tetrazine ring, short lone pair–π contacts on the same side of the s-tetrazine ring (O11···C9 and O12···C10, 3.02(1) and 3.10(1) Å, respectively). It can be easily appreciated form Figure 6 how the all-trans conformation of the ligand arms in the previously reported crystals is replaced by an arch-shape ligand conformation in the new polymorph.

As can be appreciated, the almost symmetrical all-trans conformation of the two ligands arms is lost, and a more arch-shaped arrangement, one strongly discriminating the two faces of the s-tetrazine moiety, is found instead. Ligand–anion salt-bridges are spatially rearranged accordingly, but they maintain their role of most significant interactions.

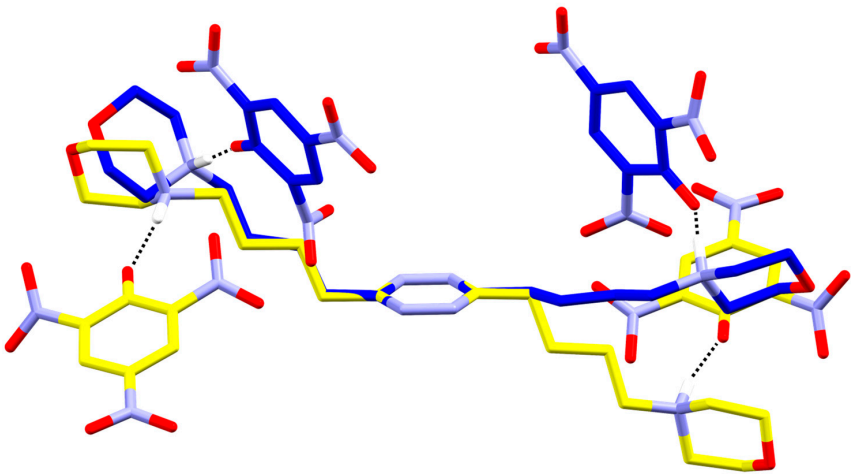

Figure 6. Comparative view of the H_2L4^{2+} conformation in its previously reported picrate complex (yellow carbon) [21] and in the new polymorph (blue carbon).

In principle, with L4 being the most flexible ligand in the series, its potential for polymorph formation could be relatively expected. What is mostly interesting about this crystal structure is that, unlike any the other of the 30+ reported crystals structures of the L1–L4 ligand series [15–21], the s-tetrazine displays a quite unexpected behavior. Only one side of the s-tetrazine is engaged in interactions (of the lone pair–π type), the convex side of the arch, while the other one, the concave side, is, surprisingly, virtually not in touch with anything.

As it can be appreciated from Figure 7, this happens mostly due to the fact that salt-bridge-bonded 1:2 ligand:anions clusters are intercalated to one another in forming a stack of head to tail interacting (π–π stacking) picrate anions. The irregular (with respect to previously reported structure) folding of the ligand makes it so that a very small pocket exists over one of the faces of the s-tetrazine ring, while the other is engaged in strong lone pair–π contacts with a nitro group (mind the significant torsion of the nitro group with respect to the benzene ring, as further discussed in ref. [21]).

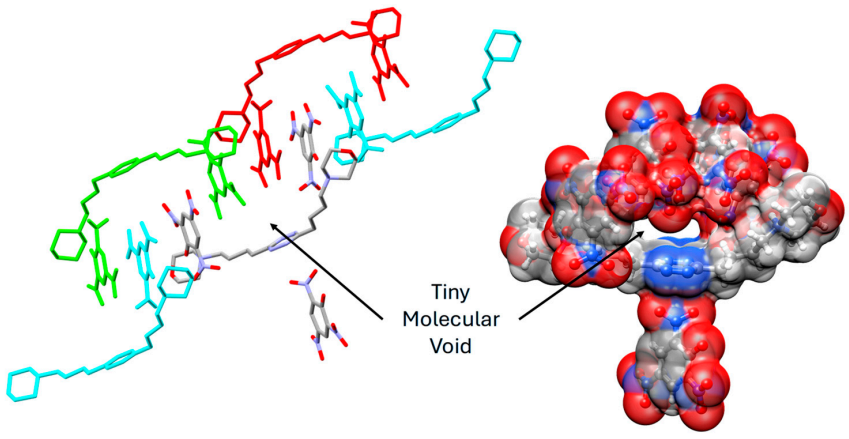

Figure 7. Packing of the new $H_2L4(picr)_2$ polymorph. Left: The salt-bridge bound picrate substrates of the deprotonated ligand (standard CPK coloring, anion–π interacting picrate on the other side also shown) form a π-stack by intercalation with the picrate anions salt-bridge bound to neighboring ligands (in cyan and green for showing purposes). Above each s-tetrazine ring, 2 non-salt-bridge-bound picrate anions to that specific ligand can be found (red and green with respect to the CPK colored ligand). Right: In order to maintain tight π–π stacking among themselves, the two red-green (left) picrate anions do not touch the s-tetrazine ring; distances among the anion and the s-tetrazine atoms are greater than the sum of van der Waals radii.

The "molecular void" is nowhere near traditional pores in terms of size (it is so small a H atom would hardly fit) and it is more a case of "inefficient packing". For this very reason, it is generally considerably difficult to engineer similar features into crystal packing. Regarding the "ineffectiveness" of the packing in the new polymorph, while the overall mutual arrangement of the molecules is more complex and it does leave, as said, these tiny—Angstrom-sized—holes, it turns out that this new packing is still overall slightly more efficient than the packing of the original compound. As a matter of fact, the calculated crystal density slightly increases, from 1.509 to 1.516 g/cm^3, with respect to the previously reported polymorph. It is possible that the low solubility of the main compound and its simpler packing justify why the polymorph cannot be easily isolated in bulk quantities.

This kind of phase is potentially of interest for current discussion in shock-induced initiation.

On the one hand, lack of intermolecular interactions, reduced layer interpenetrations, etc. . . (all possibly stemming from the presence of voids) are generally thought to reduce the shock sensitivity and self-initiations of explosives [42–44].

On the other hand, voids are considered highly dangerous, as their collapse under shock conditions is generally related to the formation of temperature hotspots in the material. Still, Angstrom-sized voids are both difficult to obtain and are not much studied, with most of the available data referring to the effect of grain boundaries [45] and nanometric, or even micrometric, voids [46–49]. To be fair, also in our case, we found no simple synthetic method to obtain the newly described L4 polymorph over the main reported one, which remains a simpler and much more accessible phase. As to why larger voids are more investigated (beyond being more common), this is due to their relevance in applications: large voids may stem, for example, from defective explosive fabrication involving binders, plasticizers, etc. . . and seriously affect the shock sensitivity of the system.

In any case, as serendipity provided, we also decided to analyze the slip planes in the new polymorph. It must be noted that most slip planes candidates are hydrogen bonded. The most significant one, i.e., the one presenting minimal layer interpenetrations, is shown below in Figure 8.

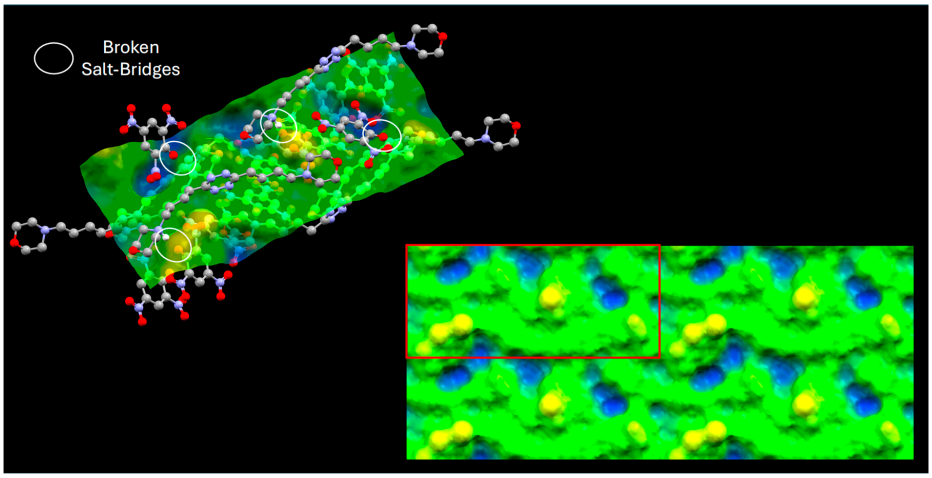

Figure 8. Less interpenetrated slip plane in the new $H_2L4(picr)_2$ polymorph. Salt-bridge rupture (white circles on the left) is required for slipping. The enlarged (4 × 4) topology shows how the peaks and valleys correspond to the regions where salt-bridges need to be torn apart.

Among the first non-hydrogen bonded planes, indeed a candidate slip planes exists which exploits the arguably easy cleaving of the non-interactions on one side of the s-tetrazine (Figure 9). Although this remains a quite interdigitated slip plane (arguably so much that friction would in any case be excessive, cf. Table 2), in principle, only anion–π

and picrate–picrate stacking contacts would need to be broken for slipping, nor much energy release is expected due to the "collapsing" of Angstrom-sized "voids".

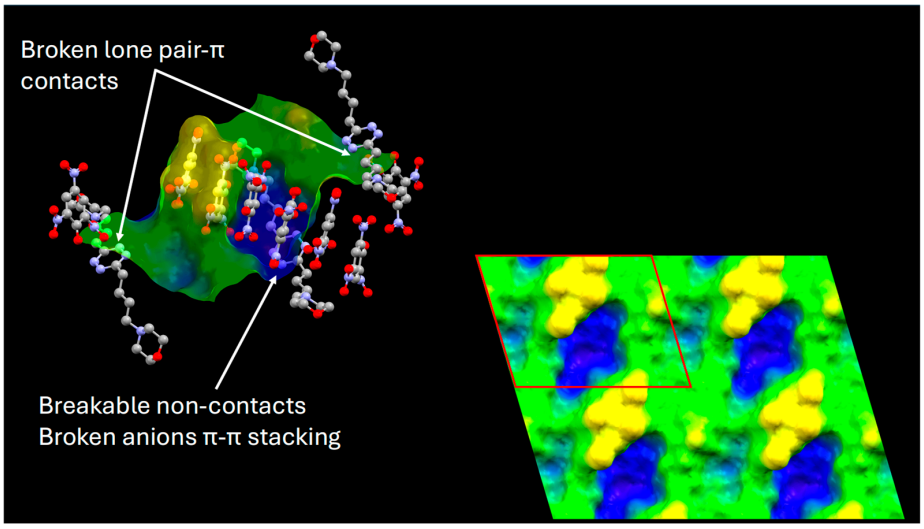

Figure 9. Slip plane cutting through the "void" over the s-tetrazine ring in the new $H_2L4(picr)_2$ polymorph. Salt-bridge rupture (details on the left) is required for slipping. The enlarged (4 × 4) topology shows how the peaks and valleys correspond to the π-stack of picrate anions.

A comparison of the features of both planes is offered in Table 2.

Table 2. Comparative features of the more relevant slip-plane candidates for the $(H_2L5)_2(picr)_4$ crystal structure.

Slip Plane	Less Interpenetrated	Non-H Bonded Passing Through the "Void" Region
Orientation	(20–4)	(020)
Offset (Å) [a]	0.000	0.000
Slab Separation (Å) [b]	−1.670	−3.488
Repeat Distance (Å)	4.512	6.488
Salt-Bridges	Yes	No
Rugosity [c]	1.312	1.558

[a] Offset in the normal direction with respect to the plane family specified as "Orientation". [b] Distance of adjacent slabs through the slip planes (negative values indicate layer interpenetration). [c] Ratio of "real" (1.2 Å probe, 0.3 Å grid spacing) surface area to projected "geometrical" area.

3.3. Thermal Analysis

Available data on the series of L1–L5 ligands are reported in Table 3.

L1–L4 and their picrate complexes were subjected to DSC/TGA analysis in a previous work [21].

The new L4 polymorph could not be studied due to insufficient material.

The analysis of the commercial L5 ligand shows an endothermic peak centered at approximately 260 °C, with an integrated enthalpy of 73 ± 5 J/g. The uncertainty associated with this measurement is substantially larger than that of the other samples (≈ ± 0.5 J/g, Table 3), indicating lower reproducibility for this system. Notably, the mass-loss signal displays two well-defined peaks corresponding to weight losses at 244 ± 2 °C and 266 ± 2 °C (Figure S2). After these thermal events, the residual mass is 0%, confirming complete decomposition of the compound. Therefore, the endothermic signal cannot be attributed to

a simple melting transition (as indicated by suppliers); instead, it reflects a more complex process involving the thermal decomposition of the material.

Table 3. Thermal analysis data, including activation energies (E_a) and preexponential factors (A) derived from the Kissinger model (R^2 correlation coefficient is also reported).

Sample	T_{INIT} (°C)	T_{ONSET} (°C)	ΔH (J/g)	E_a (kJ/mol)	A (min^{-1})	R^2
L1 [a]	181.6	222.7	378.7	-	-	-
H_2L1(picr)$_2$ [a]	182.9	215.2	1419	517	1.8×10^{52}	0.994
L2 [a]	149.3	198.1	530.9	-	-	-
H_2L2(picr)$_2$ [a]	184.6	221.2	1359	336	4.8×10^{32}	0.996
L3 [a]	148.0	201.8	694.1	-	-	-
H_2L3(picr)$_2$ [a]	190.5	233.7	1596	164	1.6×10^{13}	0.988
L4 [a]	196.1	209.7	2677	-	-	-
H_2L4(picr)$_2$ [a]	185.9	211.1	1696	153	1.4×10^{12}	0.993
H_2L5(picr)$_2$	200.1	270.1	655.3	192	1.8×10^{15}	0.990
Picric acid [a]	286.5	303.9	1694	-	-	-

[a] see ref. [21]. T_{INIT}, initial decomposition temperature; T_{ONSET}, onset temperature of the thermal event; ΔH, enthalpy of the thermal event; E_a, extrapolated activation energy of the thermal event (Kissinger equation); A, extrapolated preexponential factor of the thermal event (Kissinger equation); R^2, R-squared of the Kissinger fitting.

The L5 picrate complex was also investigated. Interestingly, it is characterized by a significant thermostability (highest T_{init} and T_{on} in the series), with interesting temperatures falling in the range of recently reported s-tetrazine-based high-energy materials specifically engineered toward that end [3]. For this compound, it was also possible to extrapolate thermokinetic parameters using the Kissinger model, as previously conducted for L1–L4 complexes. In the latter case, a trend of decreasing activation energies and increasing preexponential factors (Table 3) were found. Both in terms of activation energy (192 kJ/mol) and preexponential factor (1.8 10^{15} min^{-1}), the system ranks in-between L2 and L3 (Figure S3).

Many relevant considerations can be made; for example, that H_2L2(picr)$_2$ and H_2L5(picr)$_2$ have the same N/C ratio, or that L5 has an oxygen balance which is closest to L1 among all the ligands, or that L5 has a 15% lower MW than the shortest ligand in the series (L1), or that the L5 complex is slightly denser (about 5%) than the denser of the other analogues (L1) etc... Obtained data for L5 appear comparable to those previously reported, although the fact remains that the L5 complex cannot meaningfully remain within the marked trends elucidated for homologous ligands displaying the very same intermolecular interactions in crystals of the same composition (see below also for the important difference in standard enthalpy of formation).

3.4. In Silico Characterization of Explosion Properties

Explosion parameters calculated with EXPLO5 [50] for the picrate salts of ligands L1–L4 have been previously reported [21]. To these, the properties of the new polymorph of the L4 and L5 salts have been added.

In order to run the calculations, beyond some trivial (compound identity, formula, MW) or experimental (crystal density) parameters a required one is the ΔH_f^0 of the salt (Table 4).

Table 4. EXPLO5 [50] calculated explosion parameters.

Compound	OB (%)	D_{CJ} (km/s)	P_{CJ} (GPa)	T_{CJ} (K)	ΔH_d (kJ/g)	G (km/s)	ΔH_f^0 *
$H_2L1(picr)_2$ [a]	−97.5	6.894	17.3	2975	4.821	2.326	272
$H_2L2(picr)_2$ [a]	−106.4	6.761	16.3	2827	4.700	2.279	214
$H_2L3(picr)_2$ [a]	−114.8	6.556	14.9	2713	4.688	2.180	188
$H_2L4(picr)_2$ [a]	−122.5	6.493	14.3	2600	4.665	2.104	158
$H_2L4(picr)_{2\ new\ polymorph}$	−122.5	6.523	14.5	2598	4.670	2.107	157
$(H_2L5)_2(picr)_4$	−94.5	6.687	17.9	3224	4.603	2.318	818
TNT †	−74.0	6.941	18.8	3227	4.576	2.368	

[a] Data from ref. [21]. * ΔH_f^0 were computed as per experimental section and then used as input data for EXPLO5. † Discrepancy among calculated and experimental properties are <1% (<3% for G) for the TNT reference compound. OB, oxygen balance; D_{CJ}, Chapman–Jouguet detonation velocity; P_{CJ}, Chapman–Jouguet detonation pressure; T_{CJ}, Chapman–Jouguet detonation temperature; ΔH_d, enthalpy of detonation; G, Gurney velocity; ΔH_f^0, standard enthalpy of formation.

Accurate ΔH_f^0 data for L1–L4 salts were previously obtained by employing a combination of thermodynamic tools (Born-Haber cycles, literature and DFT data for isodesmic reactions, incremental methods for L3 and L4, where -CH_2- groups are inserted in the aliphatic arms) (cf. Section 2).

It is important to note that cation and anion formation enthalpies were calculated separately; then the lattice enthalpy in forming the salt from the gaseous ions was calculated using a formula (cf. Methods and ref. [30]) that accounts for the density of the material.

Therefore, as the different packing of the polymorph of L4 causes a slight density increase, a subtle difference is found (≈1 kJ/mol) in the formation enthalpies and thus in all derived explosion parameters.

Obtained explosion parameters for all studied compounds are as reported in Table 4.

As previously commented, data at the Chapman–Jouguet (CJ) state are those typical of high-explosives (such as TNT for comparison), with denotation velocities (D_{CJ}) of several km/s, high developed pressures (P_{CJ}) and temperatures (T_{CJ}), of course associated with the overall high energy of detonation in the kJ/g range (ΔH_d).

Differences among the two isolated phases of L4 appear small, as it must be considering that the underlying difference is approximately a 5/1000 change in their densities.

Conversely, the L5 complex has an OB closest to the L1 complex, a D_{CJ} in-between the L2 and L3 complexes, highest P_{CJ} in the series, and the second highest, after the L1 complex, detonation enthalpy in the series. In general, the new L5 well approaches the TNT reference performances.

The erratic data of L5, at least with respect to a series of homologous ligands with precise structural variations, must be understood as the result of incorporating many more significant chemical changes in the ligand molecule, which obviously reflect themselves in the product mixture generated during the explosion and on the derived physical parameters. This is also immediately reflected in the calculated ΔH_f^0 of the L5 picrate salt, which is several hundreds of kJ/mol higher compared to the other compounds. The mentioned significant thermostability of the L5 picrate complex, paired with its significant detonation performances, appear noteworthy.

Calculated values are all in a reasonable range with respect to the other compounds, and all of them appear, clearly, to be high explosives.

4. Conclusions

Summarizing the above findings, the family of high explosives obtained by joining protonated s-tetrazine based receptors and picrate anions has been further expanded. A common ground for these studies, actually their original starting point, is the fine elucidation of subtending intermolecular forces. In this sense, both crystal structures, one with an unprecedented (in this series of complexes) 2:4 stoichiometry (L5 complex), another with a non-interacting face of the s-tetrazine (L4 complex), are quite remarkable. Attention to potential slip plane candidates and their topological and supramolecular features has been provided. As for thermal analysis and in silico calculated explosion parameters, the exact trend observed for the L1–L4 series of complexes appears defied. This is so, for L5, due to its significantly different chemical nature, bringing about a much more positive ΔH_f^0, which marks it as a clear outlier in the series. In this sense, it is important to also notice how the 2 salt-bridges, 2 lone pair–π contacts per ligands "rule", as previously observed for the L1–L4 series of complexes, is no more representative of the new L4 picrate complex polymorph (2 salt-bridges, 1 lone pair–π contact per ligand). As previously suggested, the micro (molecular level) details of intermolecular interactions appear to have implications on the (very) macro properties, such as explosion parameters. With the above caveats, the picrate complex of L5 appears characterized by significant thermal stability while offering in silico detonation properties which reasonably approach the features of TNT.

Supplementary Materials: The following supporting information can be downloaded at: https://www.mdpi.com/article/10.3390/cryst16010053/s1, Table S1: Crystallographic data; Figure S1: Contact details in $(H_2L5)_2(Picr)_4$ crystals; Figure S2: HF and TG/DTG profiles of L5; Figure S3: DTG profiles of $(H_2L5)_2(Picr)_4$, Kissinger fitting.

Author Contributions: Conceptualization, M.S., M.M. and A.B.; methodology, M.S., M.D.L.d.l.T., G.P., F.R., M.P. and C.B. validation, M.S., C.B., M.P. and G.P.; formal analysis, G.P., F.R., M.P. and C.B.; investigation, M.D.L.d.l.T., M.S., M.P. and G.P.; resources M.D.L.d.l.T., M.P., F.R. and M.M.; writing—original draft preparation, M.S.; writing—review and editing, all authors; visualization, M.S. and C.B.; supervision, A.B. and M.M. All authors have read and agreed to the published version of the manuscript.

Funding: This research received no external funding.

Data Availability Statement: CCDC 2515280 ($H_2L4(picr)_2$) and 2515281 ($(H_2L5)_2(picr)_4$) contain the supplementary crystallographic data for this paper. These data can be obtained free of charge via https://www.ccdc.cam.ac.uk/structures/ (accessed on 3 January 2026) (or from the CCDC, 12 Union Road, Cambridge CB2 1EZ, UK; Fax: +44 1223 336033; E-mail: deposit@ccdc.cam.ac.uk). Raw data supporting the conclusions of this article will be made available by the authors on request.

Conflicts of Interest: The authors declare no conflicts of interest.

References

1. Fershtat, L.L. Recent Advances in the Synthesis and Performance of 1,2,4,5-Tetrazine-Based Energetic Materials. *FirePhysChem* **2023**, *3*, 78–87. [CrossRef]
2. O'Sullivan, O.T.; Zdilla, M.J. Properties and Promise of Catenated Nitrogen Systems As High-Energy-Density Materials. *Chem. Rev.* **2020**, *120*, 5682–5744. [CrossRef] [PubMed]
3. Singh, J.; Staples, R.J.; Shreeve, J.M. Coordination-Driven Safer and Sustainable Energetic Materials. *J. Mater. Chem. A* **2025**, *13*, 11475–11485. [CrossRef]
4. Yu, A.; He, X.; Shen, T.; Yu, X.; Mao, W.; Chi, W.; Liu, X.; Wu, H. Design Strategies for Tetrazine Fluorogenic Probes for Bioorthogonal Imaging. *Chem. Soc. Rev.* **2025**, *54*, 2984–3016. [CrossRef] [PubMed]
5. Wu, H.; Devaraj, N.K. Advances in Tetrazine Bioorthogonal Chemistry Driven by the Synthesis of Novel Tetrazines and Dienophiles. *Acc. Chem. Res.* **2018**, *51*, 1249–1259. [CrossRef]

6. Deb, T.; Tu, J.; Franzini, R.M. Mechanisms and Substituent Effects of Metal-Free Bioorthogonal Reactions. *Chem. Rev.* **2021**, *121*, 6850–6914. [CrossRef] [PubMed]
7. De La Garza, G.D.; Kaur, A.P.; Shkrob, I.A.; Robertson, L.A.; Odom, S.A.; McNeil, A.J. Soluble and Stable Symmetric Tetrazines as Anolytes in Redox Flow Batteries. *J. Mater. Chem. A* **2022**, *10*, 18745–18752. [CrossRef]
8. Razavi, S.A.A.; Morsali, A.; Piroozzadeh, M. Redox Metal–Organic Framework for Photocatalytic Organic Transformation: The Role of Tetrazine Function in Radical-Anion Pathway. *Inorg. Chem.* **2022**, *61*, 19134–19143. [CrossRef]
9. Joshi, S.; Raj, K.A.; Rao, M.R.; Ghosh, R. An Electronic Biosensor Based on Semiconducting Tetrazine Polymer Immobilizing Matrix Coated on rGO for Carcinoembryonic Antigen. *Sci. Rep.* **2022**, *12*, 3006. [CrossRef]
10. Aswani, R.K.; Joshi, S.; Ghosh, R.; Rajeswara, R.M. Structural Tailoring of Semiconducting Tetrazine Polymers Based Immobilizing Matrix for Superior Electronic Biosensing of Carcinoembryonic Antigen. *Polym. Adv. Technol.* **2023**, *34*, 1331–1340. [CrossRef]
11. Min, S.; Jo, D.H.; Byon, H.R.; Kwon, J.E. Unveiling the Electrochemical Reversibility of Multielectron Redox in S-Tetrazine Derivatives for Large-Capacity Electrode Materials. *ChemSusChem* **2025**, *18*, e202501876. [CrossRef]
12. Jiang, X.; Li, M.; Wang, Y.; Wang, C.; Wang, Y.; Shen, T.; Shen, L.; Liu, X.; Wang, Y.; Li, X. 1,2,4,5-Tetrazine-Tethered Probes for Fluorogenically Imaging Superoxide in Live Cells with Ultrahigh Specificity. *Nat. Commun.* **2023**, *14*, 1401. [CrossRef] [PubMed]
13. Choi, J.Y.; Check, B.; Fang, X.; Blum, S.; Pham, H.T.B.; Tayman, K.; Park, J. Photocatalytic Hydrogen Peroxide Production through Functionalized Semiconductive Metal–Organic Frameworks. *J. Am. Chem. Soc.* **2024**, *146*, 11319–11327. [CrossRef] [PubMed]
14. Savastano, M.; García-Gallarín, C.; López de la Torre, M.D.; Bazzicalupi, C.; Bianchi, A.; Melguizo, M. Anion-π and Lone Pair-π Interactions with s-Tetrazine-Based Ligands. *Coord. Chem. Rev.* **2019**, *397*, 112–137. [CrossRef]
15. Savastano, M.; Bazzicalupi, C.; Giorgi, C.; García-Gallarín, C.; López de la Torre, M.D.; Pichierri, F.; Bianchi, A.; Melguizo, M. Anion Complexes with Tetrazine-Based Ligands: Formation of Strong Anion−π Interactions in Solution and in the Solid State. *Inorg. Chem.* **2016**, *55*, 8013–8024. [CrossRef]
16. Savastano, M.; García-Gallarín, C.; Giorgi, C.; Gratteri, P.; López de la Torre, M.D.; Bazzicalupi, C.; Bianchi, A.; Melguizo, M. Solid State and Solution Study on the Formation of Inorganic Anion Complexes with a Series of Tetrazine-Based Ligands. *Molecules* **2019**, *24*, 2247. [CrossRef]
17. Savastano, M.; Bazzicalupi, C.; García, C.; Gellini, C.; de la Torre, M.D.L.; Mariani, P.; Pichierri, F.; Bianchi, A.; Melguizo, M. Iodide and Triiodide Anion Complexes Involving Anion–π Interactions with a Tetrazine-Based Receptor. *Dalton Trans.* **2017**, *46*, 4518–4529. [CrossRef] [PubMed]
18. Savastano, M.; Bazzicalupi, C.; García-Gallarín, C.; Giorgi, C.; de la Torre, M.D.L.; Pichierri, F.; Bianchi, A.; Melguizo, M. Halide and Hydroxide Anion Binding in Water. *Dalton Trans.* **2018**, *47*, 3329–3338. [CrossRef]
19. Savastano, M.; García, C.; López de la Torre, M.D.; Pichierri, F.; Bazzicalupi, C.; Bianchi, A.; Melguizo, M. Interplay between Salt Bridge, Hydrogen Bond and Anion-π Interactions in Thiocyanate Binding. *Inorganica Chim. Acta* **2018**, *470*, 133–138. [CrossRef]
20. Savastano, M.; Bazzicalupi, C.; García-Gallarín, C.; de la Torre, M.D.L.; Bianchi, A.; Melguizo, M. Supramolecular Forces and Their Interplay in Stabilizing Complexes of Organic Anions: Tuning Binding Selectivity in Water. *Org. Chem. Front.* **2018**, *6*, 75–86. [CrossRef]
21. Savastano, M.; de la Torre, M.D.L.; Pagliai, M.; Poggi, G.; Ridi, F.; Bazzicalupi, C.; Melguizo, M.; Bianchi, A. Crystal Engineering of High Explosives through Lone Pair-π Interactions: Insights for Improving Thermal Safety. *Iscience* **2023**, *26*, 107330. [CrossRef]
22. Bu, R.; Xiong, Y.; Zhang, C. π–π Stacking Contributing to the Low or Reduced Impact Sensitivity of Energetic Materials. *Cryst. Growth Des.* **2020**, *20*, 2824–2841. [CrossRef]
23. Dosch, D.E.; Reichel, M.; Born, M.; Klapötke, T.M.; Karaghiosoff, K. Investigation of Structure–Property Relationships of Three Nitroaromatic Compounds: 1-Fluoro-2,4,6-Trinitrobenzene, 2,4,6-Trinitrophenyl Methanesulfonate, and 2,4,6-Trinitrobenzaldehyde. *Cryst. Growth Des.* **2021**, *21*, 243–248. [CrossRef]
24. Bu, R.; Xie, W.; Zhang, C. Heat-Induced Polymorphic Transformation Facilitating the Low Impact-Sensitivity of 2,2-Dinitroethylene-1,1-Diamine (FOX-7). *J. Phys. Chem. C* **2019**, *123*, 16014–16022. [CrossRef]
25. Zhang, C.; Jiao, F.; Li, H. Crystal Engineering for Creating Low Sensitivity and Highly Energetic Materials. *Cryst. Growth Des.* **2018**, *18*, 5713–5726. [CrossRef]
26. Zhou, T.; Zybin, S.V.; Liu, Y.; Huang, F.; Goddard, W.A. Anisotropic Shock Sensitivity for β-Octahydro-1,3,5,7-Tetranitro-1,3,5,7-Tetrazocine Energetic Material under Compressive-Shear Loading from ReaxFF-Lg Reactive Dynamics Simulations. *J. Appl. Phys.* **2012**, *111*, 124904. [CrossRef]
27. *SAINT*; Bruker AXS Inc.: Madison, WI, USA, 2001.
28. Sheldrick, G.M. A Short History of SHELX. *Acta Crystallogr. A* **2008**, *64*, 112–122. [CrossRef]
29. Sheldrick, G.M. Crystal Structure Refinement with SHELXL. *Acta Crystallogr. C* **2015**, *71*, 3–8. [CrossRef] [PubMed]
30. Jenkins, H.D.B.; Tudela, D.; Glasser, L. Lattice Potential Energy Estimation for Complex Ionic Salts from Density Measurements. *Inorg. Chem.* **2002**, *41*, 2364–2367. [CrossRef] [PubMed]
31. Manion, J.A. Evaluated Enthalpies of Formation of the Stable Closed Shell C1 and C2 Chlorinated Hydrocarbons. *J. Phys. Chem. Ref. Data* **2002**, *31*, 123–172. [CrossRef]

32. Liu, Z.; Wu, Q.; Zhu, W.; Xiao, H. Theoretical Study of Energetic Trinitromethyl-Substituted Tetrazole and Tetrazine Derivatives. *J. Phys. Org. Chem.* **2013**, *26*, 939–947. [CrossRef]
33. NIST Chemistry WebBook. Available online: https://webbook.nist.gov/chemistry/ (accessed on 12 December 2025).
34. Good, W.D. Enthalpies of Combustion of Nine Organic Nitrogen Compounds Related to Petroleum. *J. Chem. Eng. Data* **1972**, *17*, 28–31. [CrossRef]
35. Lias, S.G.; Bartmess, J.E.; Liebman, J.F.; Holmes, J.L.; Levin, R.D.; Mallard, W.G. *Gas-Phase Lon and Neutral Thermochemistry*; American Chemical Society and the American Institute of Physics: College Park, MD, USA, 1988; Volume 17, 861p.
36. Hunter, E.P.L.; Lias, S.G. Evaluated Gas Phase Basicities and Proton Affinities of Molecules: An Update. *J. Phys. Chem. Ref. Data* **1998**, *27*, 413–656. [CrossRef]
37. Frisch, M.J.; Trucks, G.W.; Schlegel, H.B.; Scuseria, G.E.; Robb, M.A.; Cheeseman, J.R.; Scalmani, G.; Barone, V.; Mennucci, B.; Petersson, G.A.; et al. *Gaussian 09, Revision C.01*; Gaussian, Inc.: Wallingford, CT, USA, 2010.
38. Zhao, Y.; Truhlar, D.G. The M06 Suite of Density Functionals for Main Group Thermochemistry, Thermochemical Kinetics, Noncovalent Interactions, Excited States, and Transition Elements: Two New Functionals and Systematic Testing of Four M06-Class Functionals and 12 Other Functionals. *Theor. Chem. Acc.* **2008**, *120*, 215–241. [CrossRef]
39. Dunning, T.H. Gaussian Basis Sets for Use in Correlated Molecular Calculations. I. The Atoms Boron through Neon and Hydrogen. *J. Chem. Phys.* **1989**, *90*, 1007–1023. [CrossRef]
40. Spackman, P.R.; Turner, M.J.; McKinnon, J.J.; Wolff, S.K.; Grimwood, D.J.; Jayatilaka, D.; Spackman, M.A. CrystalExplorer: A Program for Hirshfeld Surface Analysis, Visualization and Quantitative Analysis of Molecular Crystals. *J. Appl. Crystallogr.* **2021**, *54*, 1006–1011. [CrossRef]
41. Macrae, C.F.; Sovago, I.; Cottrell, S.J.; Galek, P.T.A.; McCabe, P.; Pidcock, E.; Platings, M.; Shields, G.P.; Stevens, J.S.; Towler, M.; et al. Mercury 4.0: From Visualization to Analysis, Design and Prediction. *J. Appl. Crystallogr.* **2020**, *53*, 226–235. [CrossRef]
42. Zhang, Z.; Si, Y.; Yu, T.; Lai, W.; Ma, Y.; Liu, M.; Liu, Y.; Wang, B. Extra Contribution to the Crystal Stability of Insensitive Explosive TATB: The Cooperativity of Intermolecular Interactions. *Def. Technol.* **2023**, *25*, 88–98. [CrossRef]
43. Zhang, C.; Wang, X.; Huang, H. π-Stacked Interactions in Explosive Crystals: Buffers against External Mechanical Stimuli. *J. Am. Chem. Soc.* **2008**, *130*, 8359–8365. [CrossRef]
44. Ma, Y.; Zhang, A.; Zhang, C.; Jiang, D.; Zhu, Y.; Zhang, C. Crystal Packing of Low-Sensitivity and High-Energy Explosives. *Cryst. Growth Des.* **2014**, *14*, 4703–4713. [CrossRef]
45. Cai, Y.; Zhao, F.P.; An, Q.; Wu, H.A.; Goddard, W.A., III; Luo, S.N. Shock Response of Single Crystal and Nanocrystalline Pentaerythritol Tetranitrate: Implications to Hotspot Formation in Energetic Materials. *J. Chem. Phys.* **2013**, *139*, 164704. [CrossRef] [PubMed]
46. Duarte, C.A.; Hamed, A.; Drake, J.D.; Sorensen, C.J.; Son, S.F.; Chen, W.W.; Koslowski, M. Void Collapse in Shocked -HMX Single Crystals: Simulations and Experiments. *Propellants Explos. Pyrotech.* **2020**, *45*, 243–253. [CrossRef]
47. Rai, N.K.; Schmidt, M.J.; Udaykumar, H.S. Collapse of Elongated Voids in Porous Energetic Materials: Effects of Void Orientation and Aspect Ratio on Initiation. *Phys. Rev. Fluids* **2017**, *2*, 043201. [CrossRef]
48. Zhou, T.; Lou, J.; Zhang, Y.; Song, H.; Huang, F. Hot Spot Formation and Chemical Reaction Initiation in Shocked HMX Crystals with Nanovoids: A Large-Scale Reactive Molecular Dynamics Study. *Phys. Chem. Chem. Phys.* **2016**, *18*, 17627–17645. [CrossRef]
49. Zhang, Y.; Wang, T.; He, Y. Hot Spot Formation and Initial Chemical Reaction of PETN Containing Nanoscale Spherical Voids under High Shock Loading. *RSC Adv.* **2022**, *12*, 11060–11074. [CrossRef]
50. Thermochemical Computer Code EXPLO5. Available online: https://www.ozm.cz/explosives-performance-tests/thermochemical-computer-code-explo5/ (accessed on 30 March 2023).